

This item is the archived peer-reviewed author-version of:

Thermal activation of gold atom diffusion in Au@Pt nanorods

Reference:

Pedraza-Tardajos Adrián, Arslan Irmak Ece, Kumar Vished, Sánchez-Iglesias Ana, Chen Qiongyang, Wirix Maarten, Freitag Bert, Albrecht Wiebke, Van Aert Sandra, Liz-Marzán Luis M.,- Thermal activation of gold atom diffusion in Au@Pt nanorods
ACS nano - ISSN 1936-086X - 16:6(2022), p. 9608-9619
Full text (Publisher's DOI): <https://doi.org/10.1021/ACSNANO.2C02889>
To cite this reference: <https://hdl.handle.net/10067/1885400151162165141>

Thermal Activation of Gold Atom Diffusion in Au@Pt Nanorods

Adrián Pedraza-Tardajos,[#] Ece Arslan Irmak,[#] Vished Kumar, Ana Sánchez-Iglesias, Qiongyang Chen, Maarten Wirix, Bert Freitag, Wiebke Albrecht, Sandra Van Aert, Luis M. Liz-Marzán,^{*} and Sara Bals^{*}



Cite This: <https://doi.org/10.1021/acsnano.2c02889>



Read Online

ACCESS |



Metrics & More



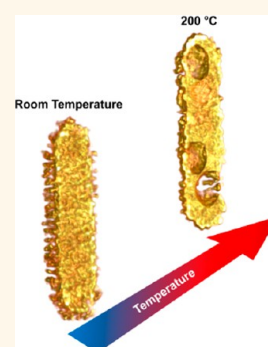
Article Recommendations



Supporting Information

ABSTRACT: Understanding the thermal stability of bimetallic nanoparticles is of vital importance to preserve their functionalities during their use in a variety of applications. In contrast to well-studied bimetallic systems such as Au@Ag, heat-induced morphological and compositional changes in Au@Pt nanoparticles are insufficiently understood, even though Au@Pt is an important material for catalysis. To investigate the thermal instability of Au@Pt nanorods at temperatures below their bulk melting point, we combined in situ heating with two- and three-dimensional electron microscopy techniques, including three-dimensional energy-dispersive X-ray spectroscopy. The experimental results were used as input for molecular dynamics simulations, to unravel the mechanisms behind the morphological transformation of Au@Pt core-shell nanorods. We conclude that thermal stability is influenced not only by the degree of coverage of Pt on Au but also by structural details of the Pt shell.

KEYWORDS: Au@Pt, bimetallic nanorods, thermal stability, in situ electron tomography, molecular dynamics simulations



Colloidal bimetallic nanoparticles (NPs) have attracted considerable interest due to the possibility to synthesize them in a wide variety of shapes and with different chemical compositions and metal distributions, so that their properties can be readily tuned for various plasmonic and catalytic applications.^{1–4} A particularly interesting type of bimetallic system comprises Au@Pt NPs, in which the excellent plasmonic properties of Au^{5,6} can be combined with the catalytic activity of Pt.⁷ This synergy has enabled applications in various fields, for example, as nanozymes,⁸ antibacterials,⁹ and catalysts for formic acid electro-oxidation.^{10,11} Since most NP properties are directly connected to their three-dimensional (3D) structure, including surface facets^{12–14} and composition,¹⁵ control over the shape and elemental distribution during synthesis is crucial.^{16–25} In some of these examples, a certain degree of order was observed, with Pt dendrites forming parallel lines over Au nanoplates.⁴ In a recent development, a micelle-directed seeded approach using chiral additives was shown to direct the growth of regular Pt spikes on the surface of Au nanorods (NRs), potentially showing chiral features.²⁶ Such systems are of great interest as they may eventually expand the applications of Au@Pt NPs into enantioselective catalysis.

Despite the interesting properties of this system, its application has been hindered by postsynthesis sensitivity to environmental conditions, such as annealing²⁵ and gaseous environments,²⁷ which often result in complex changes of the NP morphology and elemental distribution.²⁸ As a first step

toward preserving the carefully designed structure and functionalities of bimetallic NPs, we need to understand the mechanisms underlying unwanted modifications.^{29,30} Among the limited number of investigations concerning the stability of Au@Pt NRs, transmission electron microscopy (TEM) has been a preferred technique. He et al.³¹ studied the stability of Au@Pt NRs by ex situ annealing at 200 °C followed by TEM characterization. It should be noted, however, that only 2D images were acquired in this study, which in general provide insufficient information regarding complex transformations in nanostructures with 3D morphological features.³² A more direct tool for the study of morphological and compositional changes in bimetallic NPs at a local scale is in situ TEM.³³ As an alternative to the use of an environmental TEM, a wide variety of dedicated holders is available, allowing variations of gaseous environment and temperature inside the electron microscope, even in combination with 3D characterization.^{34–39}

In this context, we carried out a systematic investigation of thermal effects on the morphology and composition of Au@Pt

Received: March 23, 2022

Accepted: June 3, 2022

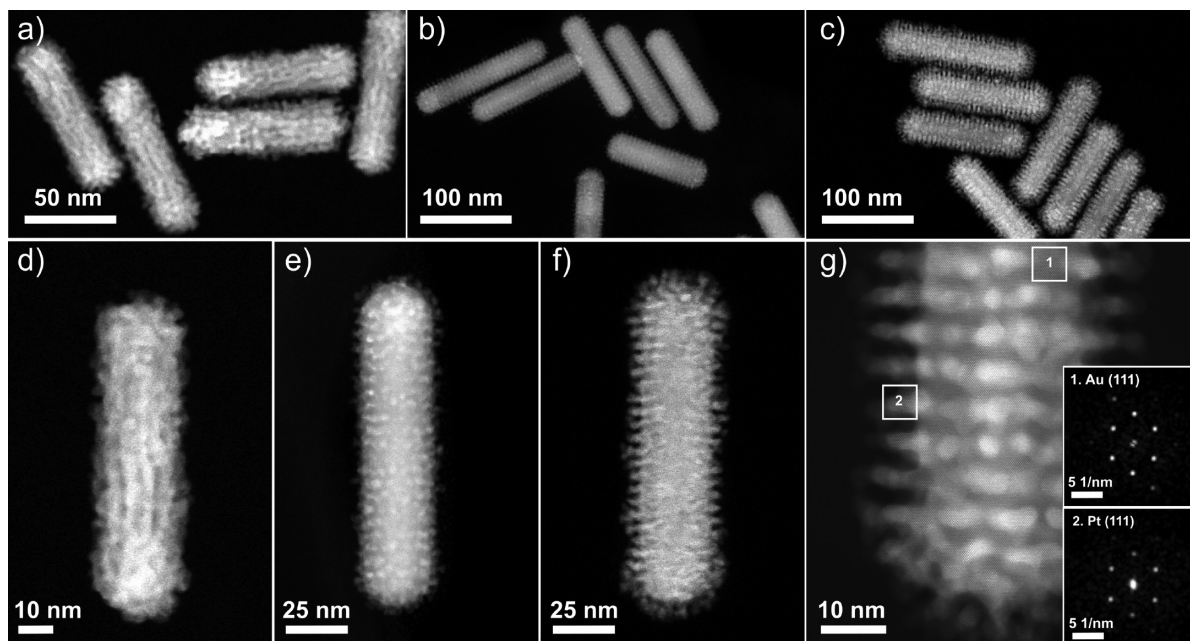


Figure 1. HAADF-STEM overview at different magnifications of the different Au@Pt NRs. (a–c) Low-magnification images of Au@Pt NRs prepared using CTAB (a) and (S)-BINAMINE/CTAC at 20 °C (b) and 40 °C (c). (d–f) High-magnification images of Au@Pt NRs shown in panels (a–c) respectively. (g) High-resolution HAADF-STEM image of the tip of an Au@Pt NR, prepared using (S)-BINAMINE/CTAC at 40 °C. The insets show Fourier transforms from the regions marked in the image by white squares, demonstrating an epitaxial relation between the Au core and the Pt shell.

NRs with different morphologies of the Pt shell, obtained by applying a surfactant-driven seed-mediated approach, either with or without chiral additives. We used electron tomography as a key tool to investigate changes in the surface features and morphology of Au@Pt NRs during in situ heating. We therefore extended earlier work on monometallic and bimetallic systems. For example, from heating studies, it is known that pure Au NRs transform into spheres at temperatures as low as 250 °C.⁴⁰ By using electron tomography, we reported that alloying in mesoporous silica-coated Au@Ag NRs started to occur within the temperature range of 300–350 °C.⁴¹ In the current study, we surprisingly observed significant changes in morphology and elemental distribution for Au@Pt NRs already at 200 °C, a temperature that is hundreds of degrees below the bulk melting temperatures of the individual elemental components (1769 °C for Pt;⁴² 1024 °C for Au⁴³). To gain a detailed understanding of the atomistic mechanisms behind the observed instabilities, we performed molecular dynamics (MD) simulations using the results from electron tomography experiments as input data. From the combined experimental and theoretical analysis, we conclude that the observed thermal instability is strongly influenced by a delicate balance between Pt shell thickness and coverage of the Au core.

RESULTS AND DISCUSSION

Synthesis and 3D Characterization of Au@Pt Nanorods. Following previous work, which focused on the preparation and surface characterization of chiral Au NRs with screw-like surface features,²⁶ we obtained Au@Pt NRs using a micelle-directed seeded-growth approach using 1,1'-binaphthyl-2,2'-diamine (BINAMINE) as a cosurfactant, together with standard cetyltrimethylammonium chloride (CTAC). To investigate the effect of the additive during Pt

overgrowth as well as to understand the role of the reaction temperature, samples were prepared with different surfactant content. Details on the synthesis are provided in the Methods section.

An overview of different samples, imaged by high-angle annular dark-field scanning transmission electron microscopy (HAADF-STEM), is presented in Figure 1. From the images, we can observe that samples grown using CTAB result in Au NRs covered with a rough Pt shell, without any regular surface features (Figure 1a,d). On the other hand, in the presence of BINAMINE, the Au@Pt NRs featured Pt rings made of spikes that grow radially outward from the central Au NR surface (Figure 1b,c). We additionally found that the length of the spikes can be tuned through the temperature used during seeded growth, as exemplified by Figure 1b,e and Figure 1c,f, which show Au@Pt NRs prepared using an (S)-BINAMINE/CTAC surfactant mixture, at reaction temperatures of 20 and 40 °C, respectively. A high-resolution HAADF-STEM image of a sample prepared at 40 °C is shown in Figure 1g and the corresponding Fourier transforms illustrate the epitaxial relation between Au and Pt.

In the remainder of this work, we will refer to these three different Au@Pt NR systems as follows: Sample (1) Au@Pt NRs synthesized using CTAB only, yielding a rough Pt shell without well-defined Pt spikes; sample (2) Au@Pt NRs synthesized using (S)-BINAMINE/CTAC (20 °C), resulting in a Pt shell composed of short spikes (2–3 nm); and sample (3) Au@Pt NRs synthesized using (S)-BINAMINE/CTAC (40 °C), resulting in a ring-like Pt shell with longer spikes (5–6 nm). The sizes of these samples were measured (including the Pt shell) and averaged over 36 particles for each system (Table 1). From these measurements, the aspect ratios for the three different samples were calculated and summarized in Table 1. Size distributions are presented in Figure S1.

Table 1. Average Morphological and Compositional Parameters of the Different Samples Investigated by HAADF-STEM and EDX at Room Temperature

sample ID	length (nm)	width (nm)	aspect ratio	[Pt/Au] ratio
(1)	96.0 ± 2.1	28.0 ± 0.7	3.43 ± 0.11	0.8 ± 0.4
(2)	140.3 ± 3.4	37.4 ± 0.7	3.75 ± 0.12	0.1 ± 0.3
(3)	148.3 ± 4.0	42.3 ± 1.1	3.50 ± 0.13	0.3 ± 0.1

The elemental distribution of the samples was investigated by energy dispersive X-ray spectroscopy (EDX). Figure 2a confirms a core-shell structure for all three samples, and Pt/Au ratios were found to range from 0.1 to 0.8, as extracted from the EDX measurements (Table 1).

Analyses of the Pt spikes at the single particle level are presented in Figure S2. These measurements suggest a regular distribution of spikes/grooves for samples (2) and (3). However, as these results were obtained from single 2D HAADF-STEM images, HAADF-STEM tomography was additionally performed to investigate the 3D morphology of the Pt shell. 3D visualizations of the electron tomography reconstructions are shown in Figure 2b, which confirm the presence of regularly arranged spikes for samples (2) and (3), whereas sample (1) contains a rough (disordered) Pt shell. 3D animations of the reconstructions are presented as Movies S1–S3. From a careful analysis of the 3D reconstructions, it is suggested that parts of the Pt spikes in (3) display quasi-helical distributions (see Movie S3). For sample (2), the spikes are too short to enable a clear interpretation. For the present work, the degree of chirality is irrelevant and the surface coverage over the Au NR core is most important.

The difference in atomic number Z for Au and Pt is too small to generate sufficient contrast in a 3D HAADF-STEM reconstruction. Therefore, to visualize the Au–Pt interface and investigate the coverage of Au by Pt in more detail, we acquired an EDX-STEM tilt series by exploiting the high efficiency of a recently developed Ultra-X EDX detector.⁴⁴ More details are provided in the Methods section. A 3D visualization of the EDX-STEM tomography reconstruction of

a representative Au@Pt NR, prepared in the presence of (S)-BINAMINE/CTAC, is presented in Figure 2c and in Movie S4. The high signal-to-noise ratio of the EDX-STEM tomography reconstruction enabled us to conclude that the Pt shell is solely composed of Pt spikes, directly grown on the Au surface, with no intermediate Pt layer present at the surface of the Au rod, in agreement with the templating effect of helical micelles on the Au NR surface, as postulated in ref 26. Based on these insights, it became possible to quantify the surface coverage for samples (2) and (3) by analyzing orthoslices through HAADF-STEM reconstructions. Hereby, Au and Pt were distinguished based on their morphological appearance. For both samples (2) and (3), it was found that approximately 2/3 of the Au NR surface was covered by Pt spikes. It should be noted that the higher [Pt/Au] ratio for sample (3) is due to the presence of longer Pt spikes, not due to a higher surface coverage.

Thermal Instability of Au@Pt NRs. Heat-induced morphological transformations were studied in situ in the TEM. Au@Pt NRs from samples (1–3) were deposited on a dedicated silicon nitride (Si_3N_4) MEMS heating chip of a DENSsolutions Wildfire heating tomography holder⁴⁵ and were heated up to 200 °C (temperature selected to compare our in situ analysis with ex situ results from ref 31). After keeping the temperature at 200 °C for 5 min, heating was switched off, and the temperature was reduced to room temperature (within ~ 1 s) to prevent further transformations while imaging. HAADF-STEM images (Figure 3, left column) illustrate the heat-induced formation of indentations or voids in all three samples. Such voids were especially noticeable in sample (3), whereas a smaller one is indicated by an arrow for sample (1). Movie S5, acquired for sample (3) during in situ heating, demonstrates that the voids started forming from indentations at the surface of the Au NR and then protruded into the core structure. Sample (2) mostly showed indentations, rather than voids. Based on 2D images (see more examples in Figure S3), we estimated that at least 23% of the total number of particles in sample (1) exhibited

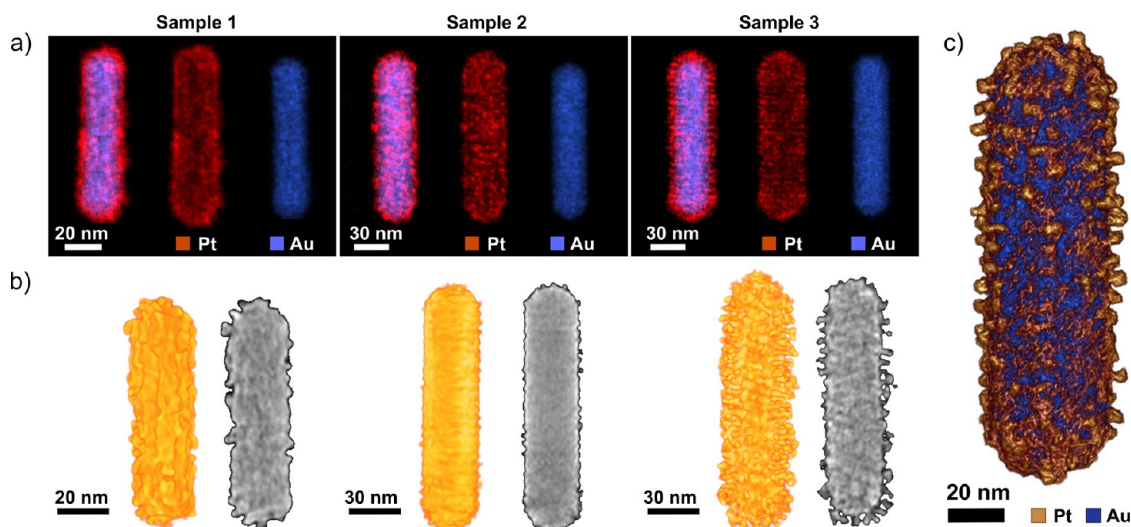


Figure 2. (a) EDX-STEM maps of Au@Pt NR samples (1), (2) and (3), with different [Pt/Au]; molar ratios calculated from EDX-STEM data are 0.8, 0.1 and 0.3, respectively. (b) 3D visualizations and orthoslices through the 3D HAADF-STEM reconstructions. (c) 3D visualization of the EDX-STEM tomography reconstruction obtained from a representative sample prepared using the BINAMINE/CTAB surfactant mixture.

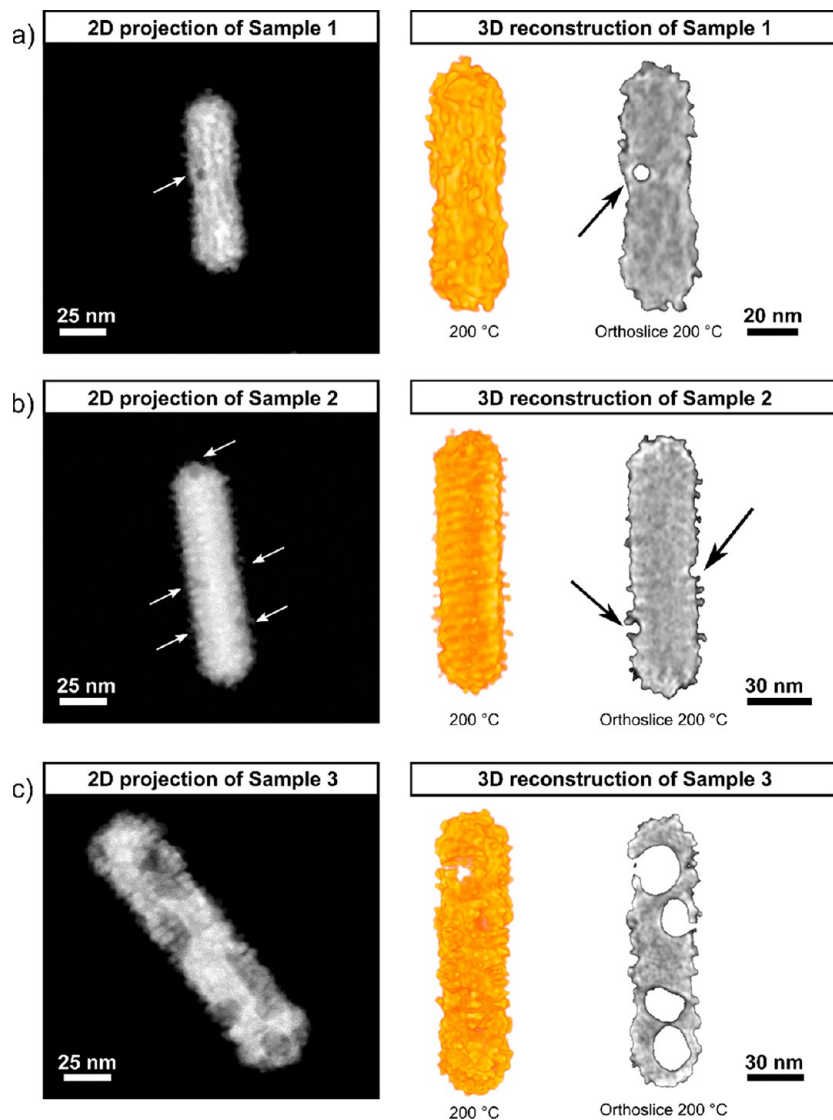


Figure 3. In situ heating tomography experiments. 2D projections, 3D visualizations, and selected orthoslices through the HAADF-STEM reconstructions obtained for the selected samples (as labeled), after heating at 200 °C for 5 min. Small voids and indentations observed in samples (1) and (2) are marked in the 2D projection images by white arrows and by black arrows in the orthoslices.

200 indentations and/or voids upon heating, whereas all NRs
 201 analyzed in samples (2) and (3) showed the presence of voids.
 202 A better understanding of this complex transformation
 203 required additional investigation in 3D, which was achieved by
 204 using in situ electron tomography.^{34–39} The results are
 205 presented in Figure 3 and animated versions of the 3D
 206 reconstructions are included as Movies S6–S8. From the
 207 orthoslices through the 3D reconstructions of sample (1),
 208 which originally had a rough, but continuous Pt shell, we
 209 observed small voids, close to the surface, along with narrow
 210 channels connecting the void to the surface (Figure 4). For all
 211 samples, depleted Au was found to form Au clusters on the
 212 otherwise empty regions of the Si₃N₄ support (Figure S4a,b),
 213 as confirmed by EDX-STEM (Figure S4c,d). Based on these
 214 observations, we hypothesize that the observed channels
 215 formed a pathway for Au atoms to diffuse out of the core,
 216 which ultimately resulted in the creation of voids inside the Au
 217 NRs, in agreement with the postulation by He et al.³¹
 218 On the other hand, sample (2) did not contain any voids
 219 inside the NR, but indentations were clearly observed at

several sites on the particle surface (marked by arrows in 220
 Figure 3b). As suggested by supporting Movie S5, it is likely 221
 that these indentations correspond to early stages in the 222
 formation of larger voids, as those observed for sample (2) 223
 For the latter sample, we observed that such large voids extended 224
 far inside the NP (Figure 3c), which made us wonder about 225
 the integrity of the Pt shell. Therefore, we performed EDX 226
 measurements (Figure S5), which demonstrated that a Pt shell 227
 is still present, despite the large voids inside the Au NR. 228

Since the degree of void formation significantly varied for 229
 different samples, we wondered whether the local Pt surface 230
 morphology plays any role on Au migration. However, the 231
 details of the underlying processes are difficult to understand 232
 from the experimental observations only. To gain insight into 233
 these mechanistic details, we performed MD simulations. The 234
 embedded atom model (EAM) was used to define the 235
 interaction between atoms, and a time step of 1 fs was used 236
 to track the movements of atoms.⁴⁶ To perform these 237
 simulations using realistic input models, we used the 238
 experimentally measured morphologies for samples (1–3) as 239

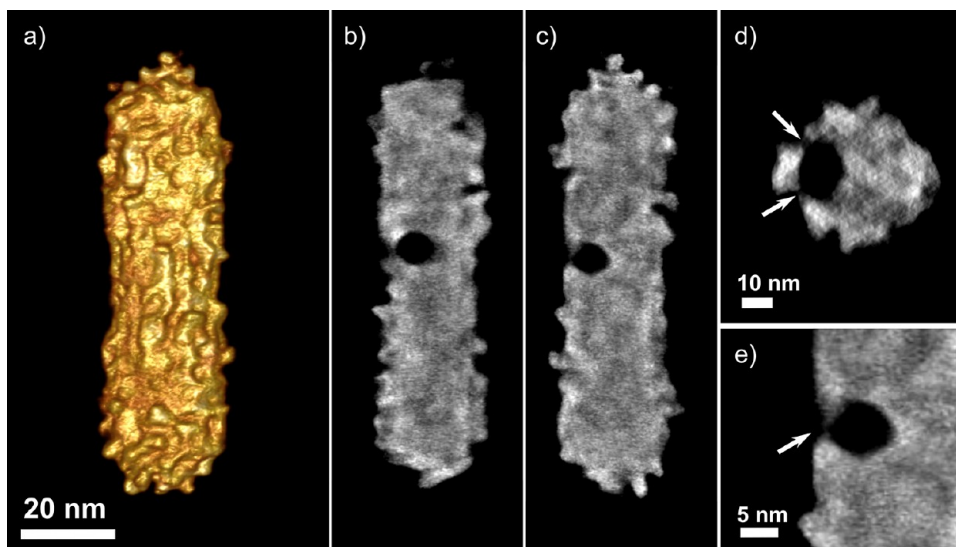


Figure 4. 3D reconstruction of an Au@Pt NR from sample (1) after heating at 200 °C. (a) 3D visualization of HAADF-STEM tomography. (b, c) Orthoslices through the 3D reconstruction along the xz and yz planes, respectively. (d) Orthoslice (xy plane) through the 3D reconstruction, showing the presence of diffusion pathways for Au atoms (marked by white arrows). (e) Magnified region from panel (c), again showing the presence of a channel through which Au atoms can diffuse out of the NR (marked by a white arrow).

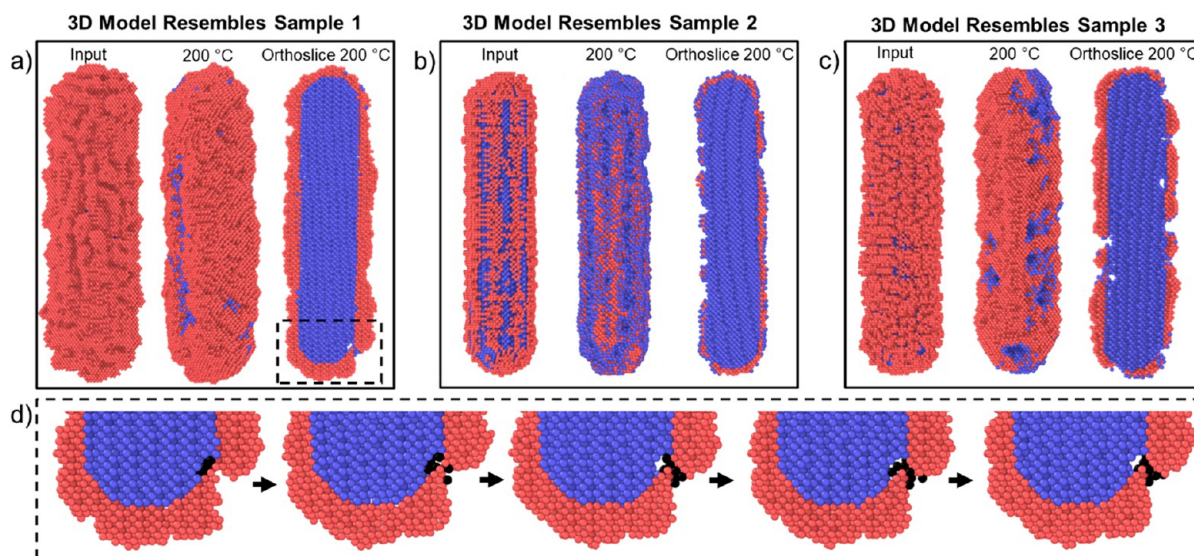


Figure 5. MD simulations based on electron tomography reconstructions. (a–c) Tomography-based 3D models and orthoslices of Au@Pt NRs before and after heating at 200 °C, resembling samples (1), (2), and (3), as represented in Figure 2b. Pt atoms are shown in red and Au atoms in blue. (d) Snapshots of the intermediate steps during the transformation of the NR in (a). Black dots represent Au atoms migrating toward the NR surface during heating at 200 °C.

240 input data (Figure 2b). Based on earlier work⁴⁷ and electron
 241 tomography reconstructions obtained for the Au NRs used as
 242 seeds (Figure S6), the Au NR was constructed to have eight
 243 {520} lateral facets and a combination of {100}, {110}, and
 244 {111} facets at the tips. Due to the time-scale limitations of
 245 MD simulations, we scaled down the overall size of the NR,
 246 but for all the other parameters such as aspect ratio and Pt
 247 coverage, experimentally determined values were used. First,
 248 the NRs were relaxed for 20 ns at room temperature.
 249 Subsequently, to mimic the experimental observations, the
 250 temperature was increased with a constant heating rate of 0.5
 251 K/ps and relaxed for 20 ns at 200 °C. All details on the
 252 simulations can be found in the Methods section.

253 In Figure 5a–c, the resulting 3D morphologies based on
 254 samples (1–3) are shown before and after heating as well as

orthoslices through the simulated NRs after heating. 255
 Indentations were observed for all samples, indicating a good 256
 agreement between experiments and simulations. It should be 257
 noted that the sizes of these indentations, appearing during 258
 MD simulations, are relatively small compared to those 259
 observed experimentally. This apparent discrepancy is related 260
 to the limited time scale used during MD simulations. It 261
 should also be noted that our simulations were performed 262
 without the presence of a Si₃N₄ sample support and with the 263
 constraint of keeping the total volume of the NRs constant, 264
 which explains why indentations rather than voids are formed. 265
 However, the good agreement between the experimental 266
 observations and simulations demonstrates that the absence of 267
 support does not change the physics of the observed 268
 transformations. 269

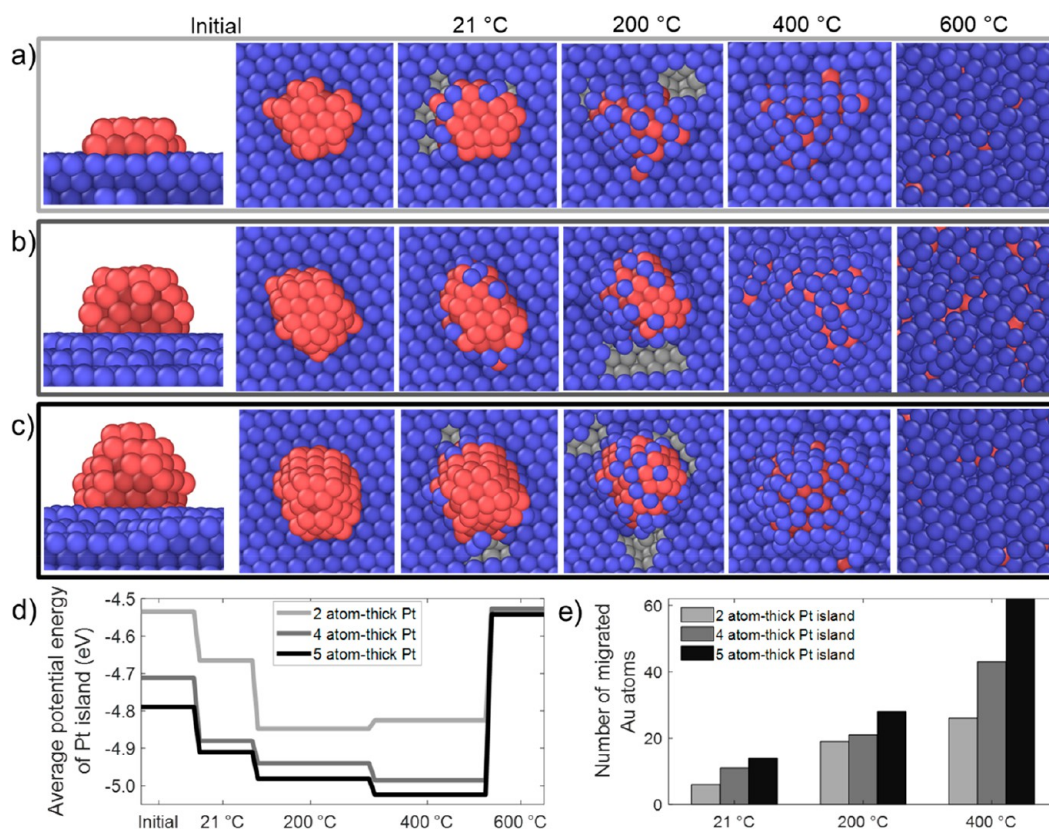


Figure 6. Effect of the thickness of Pt(111) islands on the number of Au atoms migrating to the surface of Au@Pt NRs. Pt atoms are presented in red and Au atoms in blue and voids in gray. (a–c) Side-views of 2, 4, and 5 atoms-thick Pt islands, and top views illustrating their structural evolution as a function of temperature. (d) Average change of potential energy per Pt atom in the islands as a function of temperature. (e) Histogram of the number of migrated Au atoms as a function of temperature and thickness of the simulated Pt islands.

270 The simulations allowed us to capture the *dynamics* of void
 271 formation, which could not be extracted from the experiments,
 272 in which only the structure before and after heating could be
 273 investigated. The MD results in Figure 5d demonstrate that Au
 274 atoms close to the Au–Pt interface (indicated in black for
 275 better visualization) tend to create diffusion channels and
 276 migrate toward the NR surface during heating, as hypothesized
 277 from the experimental results. This process resulted in the
 278 formation of a small indentation, as shown in Figure 5a–c. MD
 279 simulations further showed that during heating at 200 °C, 2.8%
 280 of Au atoms in sample (1) (Figure 5a) migrated to the NR
 281 surface, whereas this percentage increased to 8.2% for sample
 282 (2) and 9.0% for sample (3) (Figure 5b,c). As expected, it can
 283 also be seen that higher percentages of Au migration lead to
 284 larger indentations. Figure 5 additionally suggests that the size
 285 and location of the indentations vary for different samples,
 286 again in agreement with the experimental observations. For
 287 instance, it can be seen that the NR in Figure 5c, which had a
 288 Pt coverage of the Au core surface (Pt surface coverage) of
 289 65% (to mimic sample (3)), yielded more indentations than
 290 the NR in Figure 5a, which was simulated to have a 99%
 291 surface coverage to mimic sample (1). In addition to surface
 292 coverage, also the thickness of the Pt spikes appears to play a
 293 role during Au migration. The NR in Figure 5b, with short
 294 spikes mimicking sample (2), yielded smaller indentations at
 295 200 °C in comparison to the NR in Figure 5c, which initially
 296 had thicker spikes but a similar coverage of the Au surface, in
 297 agreement with sample (3). The good agreement between
 298 simulations and experimental observations confirms that the
 299 MD approach can be used to better understand the

mechanistic processes behind the thermal instability of Au@ Pt NRs.

As a next step, we decoupled the morphological parameters of the Pt shell, namely surface coverage and thickness of Pt spikes. To investigate the latter, different Pt islands, mimicking Pt spikes, were placed on an Au(111) surface, and temperature was gradually increased (Figure 6). All islands had the same Au–Pt interfacial area, but each of them had a different height corresponding to 2, 4, or 5 atomic layers. Side- and top-views of these islands are presented in Figure 6a–c, as a function of temperature. Already at room temperature, Au atoms were observed to move to the top of the Pt islands, regardless of the island thickness. As a result, small indentations were formed at the surface (as indicated by gray dots). However, after 10 ns, this process was not seen to propagate any further. Next, the temperature was increased to 200 °C with a 0.5 K/ps heating rate and the system was relaxed for 20 ns. We clearly observed that the higher temperature significantly enhanced Au migration toward the top of the Pt islands, resulting in larger indentations at the Au surface.

Because of larger thermal vibrations, it is typically expected that the potential energy of a system monotonically increases with increasing temperature, prior to reaching its melting point. On the contrary, Figure 6d shows that the average potential energy of the Pt atoms decreased as temperature was increased from room temperature to 400 °C. These observations can be rationalized from a thermodynamics point of view. Recent studies revealed that the cohesive energy and Wigner–Seitz radius, which is defined as the radius occupied by one atom,⁴⁸ are the two primary factors affecting

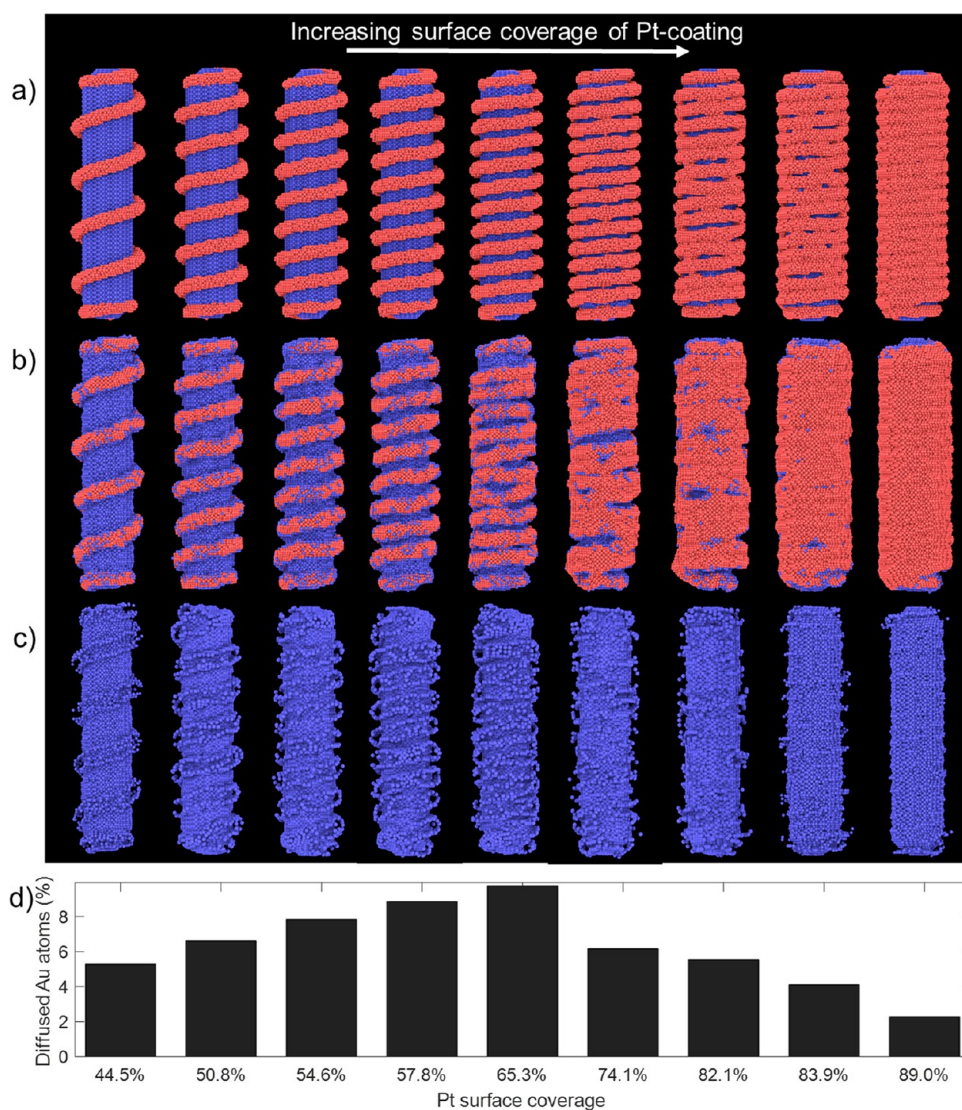


Figure 7. Surface-coverage effect of the Pt shell around the Au NR, on the number of migrated Au atoms. (a) Created input structures. (b) Structures after heating at 200 °C. (c) Au atoms within the Au@Pt NR after heating to 200 °C. (d) Percentage of migrated Au atoms from structures with different Pt surface coverage.

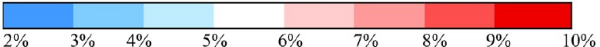
330 the preference for an element to be at the core or the shell in
331 bimetallic NPs.^{49–51} In general, the less cohesive element, with
332 a larger Wigner–Seitz radius, prefers to segregate at the
333 surface. In our case, Au is less cohesive than Pt, with cohesive
334 energies of -2.88 eV and -5.19 eV, as determined from MD
335 simulations for spherical Au and Pt NPs, respectively (Table
336 S1). Moreover, Au has a larger Wigner–Seitz radius (3.01
337 Bohr radius) than Pt (2.90 Bohr radius),⁵² and hence Au
338 prefers to migrate toward the surface to reduce strain at the
339 Au–Pt interface and consequently minimize the overall energy
340 (Figure 6d). This hypothesis is supported by MD simulations
341 of Au@Pt and Pt@Au NPs (Figure S7). It is important to note
342 that the formation of indentations at the Au surface (Figure
343 6a–c) prevailed at mild temperatures only. When the
344 temperature was increased further to 400 °C and above, we
345 observed that the voids diminished since a higher thermal
346 vibration results in larger spacing between Au atoms at the
347 surface. This was followed by surface melting (sharp potential
348 energy increase in Figure 6d) at 600 °C. It should be noted
349 that in our experiments Au atoms migrated to the Si_3N_4 grid
350 rather than the top of the Pt spikes.

As a consequence of the thermodynamic instability, thicker
Pt islands induced the formation of larger indentations on the
Au surface, as more Au atoms were required to cover the
thicker Pt-islands. Figure 6e illustrates the increase in the total
number of migrated Au atoms as a function of temperature, for
each system. This explains why the voids became more
pronounced in our experiments for samples with larger Pt
spikes (sample (3)).

Next, the influence of Pt surface coverage was investigated.
Based on the electron tomography experiments at room
temperature, we created Pt-coating replicating samples (2) and
(3) (see Figure 2). Since the particles showed regions in which
the Pt spikes showed a quasi-helical arrangement, we decided
to model the Pt surface coverage in a systematic manner by
changing the number of Pt helical turns at the surface of a Au
NR. As a result, Au@Pt NRs with different Pt surface coverage,
ranging from 44.5% to 89%, were obtained (left to right in
Figure 7a). The Pt surface coverage was defined as the ratio
between the number of Au surface atoms covered by the Pt
shell and the total number of atoms at the surface of the Au
core. The structures obtained after heating at 200 °C are 371

Table 2. Percentage of Diffused Au Atoms after Heating at 200 °C by MD Simulations for Au@Pt NRs with Different Pt Surface Coverage and Thickness of the Pt Shell

		Surface Coverage of Pt Shell									
		44.5%	50.8%	54.6%	57.8%	65.3%	74.1%	82.1%	83.9%	89.0%	100%
Thickness of Pt shell ↓	2 atom-thick	4.9 %	6.4 %	7.2 %	8.1 %	9.7 %	9.8 %	9.2 %	7.6	3.3	2.0 %
	3 atom-thick	5.1 %	6.6 %	7.2 %	8.1 %	9.7 %	7.3 %	5.6%	3.4	2.0	0.5 %
	4 atom-thick	5.1 %	6.5 %	7.4 %	8.5 %	9.6 %	6.3 %	5.4%	3.8	2.2	0.0 %
	5 atom-thick	5.3 %	6.8 %	7.8 %	8.9 %	9.8 %	6.2 %	5.5 %	4.1 %	2.3 %	0.0 %



372 shown in Figure 7b, along with a visualization of Au atoms
 373 only (Figure 7c). The resulting percentages of Au atoms that
 374 migrated from the core to the surface of the Pt shell are plotted
 375 in Figure 7d. This percentage was defined as the ratio between
 376 the number of migrated Au atoms and the total number of
 377 atoms in the Au core. Since the same Au core was used for all
 378 Au@Pt NRs in Figure 7, these percentages can also be
 379 interpreted in an absolute manner. As the Pt surface coverage
 380 increased from 44.5% to 65.3%, the number of migrated Au
 381 atoms increased, as expected from our previous results,
 382 demonstrating the tendency of Au atoms to cover the Pt
 383 islands. However, for Pt coverages higher than 65.3%, a
 384 decrease in the number of migrated Au atoms was observed.
 385 This is not surprising, since higher Pt coverage allows less Au
 386 diffusion pathways between Pt spikes. Consequently, for an
 387 Au@Pt NR with 89% Pt coverage, the number of Au atoms
 388 that could migrate upon heating was significantly reduced, and
 389 the initial shape of the core of the Au NR was almost fully
 390 preserved after heating.

391 Finally, to understand the interplay between surface
 392 coverage and thickness of the spikes, MD simulations were
 393 carried out for different Pt coatings by varying both the surface
 394 coverage and the thickness of the Pt islands. The results of the
 395 simulations for 40 combinations of different morphologies are
 396 summarized in Table 2, in the form of the percentage of
 397 diffused Au atoms at 200 °C. The corresponding input
 398 structures used for the simulations are additionally shown in
 399 Figure S8. For the sake of visualization, the results in Table 2
 400 are color-coded, with red representing the largest number of
 401 diffused Au atoms and blue corresponding to negligible
 402 migration of Au atoms. Two different trends can be observed
 403 from this table. At Pt surface coverages below 74%, an
 404 increasing number of Pt atoms, in terms of either surface
 405 coverage or thickness of the Pt islands, resulted in a higher
 406 percentage of migrated Au atoms. Therefore, the highest
 407 percentage of Au diffusion was observed for NRs with 65% Pt
 408 surface coverage and 5 atom-thick Pt dendrites. This system
 409 had sufficiently long Pt spikes to stimulate the diffusion of Au
 410 atoms, while yielding sufficient Pt-free Au surface to enable Au
 411 migration. On the other hand, once the Pt surface coverage
 412 reached 74%, fewer Au atoms could diffuse because of the lack
 413 of Pt-free pathways. Obviously, this effect was most dominant
 414 for NRs with a continuous Pt shell (rightmost column), for

415 which Au atoms would have to create diffusion channels
 416 toward the surface and thus overcome the energy barrier
 417 imposed by the Pt shell. As illustrated in Figure S9, this is only
 418 possible for a thin Pt shell (2 atom layer thick). Our combined
 419 results indicate that Au surfaces with a high Pt coverage
 420 significantly improve the thermal stability of Au@Pt NRs,
 421 especially for large spikes, due to a stronger kinetic trapping
 422 effect against heat-induced atom migration.

CONCLUSIONS

423 All of these results contribute to understanding the driving
 424 forces behind Au migration and the resulting thermal
 425 instability of Au@Pt NRs. We demonstrated that experimen-
 426 tally observed heat-induced transformations depended on
 427 morphological details of the nanostructure, with Pt surface
 428 coverage and thickness of Pt spikes being the main factors
 429 influencing thermal instability. At elevated temperatures, Au
 430 atoms diffused from the core to the surface of the Pt shell to
 431 reach a thermodynamically more stable configuration, with Pt
 432 spikes acting as the nucleation sites for Au atoms. Longer Pt
 433 spikes led to an increased number of migrated Au atoms and
 434 consequently larger voids. However, this process was mainly
 435 dominated by the continuity of the Pt shell. At Pt surface
 436 coverages exceeding 74%, the Pt coating was found to act as a
 437 barrier against Au atom diffusion, thereby reversing the
 438 mechanism: Longer Pt spikes led to a decrease in the
 439 percentage of diffused Au atoms.

440 There is general agreement with literature reports showing
 441 that core-shell formation in Pt-Au bimetallic NPs is affected
 442 by the atomic size and cohesive energy of the constituent
 443 elements.^{49–53} In addition to such previous reports, our
 444 findings show that heat-induced deformation at mild temper-
 445 atures can be explained by a delicate interplay between
 446 thermodynamics and kinetics. Our work provides an atomistic
 447 insight toward tuning the thermal stability of Au@Pt NPs by
 448 changing the morphology of Pt shells, for relevant applications
 449 at which elevated temperatures are needed.

450 In conclusion, combined results from electron microscopy
 451 and MD simulations enabled us to understand the thermody-
 452 namic behavior of Au@Pt NPs, involving a complex
 453 cooperative effect between Au and Pt at the atomic scale.
 454 Our experiments revealed that Au@Pt NRs exhibited structural
 455 deformation at temperatures well below the melting point of
 456

457 both Au and Pt, creating voids and indentations in the Au core.
458 We observed that such structural transformations largely
459 depended on the morphology and coverage of the Pt shell.
460 MD simulations enabled us to conclude that the observed
461 deformations take place because the system aims to reduce its
462 total energy by migration of Au atoms from the core through
463 the interface to the outer surface, leading to a thermodynamically
464 favorable structure. Our findings can be ultimately
465 exploited to improve the design of these systems to preserve
466 their functionalities for electro- and photocatalytic applications
467 operated at elevated temperatures.

468 METHODS

469 **Colloidal Synthesis of Au@Pt NRs.** *Materials.* Hexadecyltrimethylammonium bromide (CTAB, $\geq 99\%$), hydrogen tetrachloroaurate trihydrate (HAuCl_4 , $\geq 99.9\%$), silver nitrate (AgNO_3 , $\geq 99\%$), L-ascorbic acid (AA, $\geq 99.0\%$), sodium oleate (NaOL , $\geq 99\%$), *n*-decanol (98%), (R)-(+)-1,1'-binaphthyl-2,2'-diamine ((R)-BIN-AMINE, 99%), (S)-(–)-1,1'-binaphthyl-2,2'-diamine ((S)-BIN-AMINE, 99%), sodium borohydride (NaBH_4 , $\geq 96\%$), hydrochloric acid (HCl, 37%), and potassium tetrachloroplatinate (II) (K_2PtCl_4 , 98%) were purchased from Aldrich and used without further purification. Hexadecyltrimethylammonium chloride (CTAC, 99%) was purchased from ACROS Organics. Milli-Q water (resistivity 18.2 $\text{M}\Omega\text{-cm}$ at 25 °C) was used in all experiments. All glassware was washed with aqua regia, rinsed with Milli-Q water, and dried before use.

483 *Synthesis of Au@Pt Nanorods with Continuous Pt Shell.*
484 *Synthesis of Gold Nanorods.* Au NRs were prepared through the seeded growth method,⁵⁴ based on the reduction of HAuCl_4 on CTAB-stabilized Au nanoparticle seeds in the presence of silver ions. Gold seeds were prepared by fast reduction of HAuCl_4 with NaBH_4 in CTAB solution. A certain volume of HAuCl_4 solution (0.025 mL, 50 mM) solution is added to a solution of CTAB (4.7 mL, 100 mM). Afterward, a freshly prepared NaBH_4 (0.3 mL, 10 mM) solution is rapidly injected under vigorous stirring. The solution color changed from yellow to brownish yellow, and the stirring was stopped after 2 min. The gold seed solution was aged at room temperature for 30 min before use. To prepare the growth solution, 9.0 g of CTAB and 1.234 g of NaOL were dissolved in 500 mL of warm Milli-Q water (~50 °C) in a 1 L Erlenmeyer flask. Once the sodium oleate is completely dissolved, the mixture was cool down to 30 °C, and AgNO_3 (24 mL, 4 mM) was added under stirring. The mixture was kept at 30 °C for 15 min after which HAuCl_4 was added (2.5 mL, 100 mM) under vigorous stirring. The mixture became colorless after 20 min at 30 °C, and HCl (2.1 mL, 37%) was introduced. After 15 min of stirring, AA (1.25 mL, 64 mM) was added, and the solution was vigorously stirred for 30 s. Finally, a certain volume of seed solution (0.8 mL, 0.25 mM) was injected into the growth solution under vigorous stirring for 5 min, and then the solution was left undisturbed at 30 °C for 12 h. The solution was centrifuged twice (8000 rpm, 30 min) to remove excess reactants and dispersed in aqueous CTAB solution (100 mM).

508 *Platinum Overgrowth.* For platinum deposition, a previously reported method was followed.¹⁸ To a dispersion of Au NRs (10 mL) containing CTAB (100 mM) and metallic gold (0.25 mM) at 40 °C were added K_2PtCl_4 (0.05 mL, 50 mM) and AA (0.5 mL, 100 mM) under vigorous stirring for 5 min. The mixture was left undisturbed at 60 °C for 12 h. Finally, the obtained solution was centrifuged twice and redispersed in water.

515 *Synthesis of Au@Pt Nanorods with Discontinuous Pt Shell.*
516 *Preparation of Gold Nanorods.* The Au NRs were prepared using a modified seed-mediated approach.⁵⁵ To prepare Au seeds, 20 mL of a solution 13.5 mM in *n*-decanol and 50 mM in CTAB was poured in a 50 mL glass beaker. To this solution, 200 μL of 50 mM HAuCl_4 and 100 μL of 100 mM AA were added sequentially, under slow stirring to reduce Au (III) into Au (I), as confirmed by the change in the solution color from yellow to colorless. Finally, 800 μL of freshly prepared 20 mM NaBH_4 solution was added to the above solution

under vigorous stirring, and the obtained Au seed solution was aged for 60 min at room temperature.

Small Au NRs were then prepared as follows: 1 mL of 50 mM HAuCl_4 , 0.8 mL of 10 mM AgNO_3 , 65 mL of 1 M HCl, and 1.3 mL of 100 mM AA were added to 100 mL of a solution of *n*-decanol (13.5 mM) and CTAB (50 mM) at room temperature, under mild stirring. After 1 min, 6 mL of Au seed solution was added to this mixture. After small Au NR growth (ca. 4 h), 50 mL of the resulting solution was centrifuged at 7000 rpm for 15 min, to precipitate large NPs, and then the supernatant (containing small Au NRs) was collected and centrifuged at 14,500 rpm for 45 min in 2 mL Eppendorf tubes. The precipitate was collected and redispersed using 10 mM CTAB stock solution. The final small Au NR concentration was set to 4.5 mM (Au). The as-synthesized small NRs were 21 nm in length and 7.5 nm in width, with an LSPR band at ~720 nm. For synthesis of larger Au NRs, 1 mL of 50 mM HAuCl_4 , 1.5 mL of 10 mM AgNO_3 , 12 mL of 1 M HCl, and 0.8 mL of 100 mM AA were added to 100 mL of a mixed solution of *n*-decanol (11 mM) and CTAB (50 mM) in a 250 mL Erlenmeyer flask. Under mild stirring, 45 μL of small Au NR solution was added and left undisturbed overnight at 16 °C. The resulting Au NRs were 130 nm in length and 29 nm in width, with an LSPR band at ~930 nm. These Au NRs were washed multiple times by centrifuging at 3500 rpm and redispersing the precipitate in 10 mM CTAC stock solution.

These Au NRs were used as seeds to grow a stripy Pt shell, following a published protocol.²⁶

Preparation of BINAMINE/CTAC Solution. In a 40 mL glass vial, 0.96 g of pure CTAC and a fixed amount of chiral cosurfactant were weighed. To this mixture, 30 mL of water was added and then heated to 60 °C for 3–4 h, under mild stirring. This solution was then cooled down to room temperature and stored in a dark place until further use. The final concentrations of BINAMINE and CTAC were fixed to 2.5 mM and 100 mM, respectively.

Washing and Incubation in BINAMINE/CTAC Solution. A small amount of as-synthesized Au NR solution [$[\text{Au}^0] \sim 5 \text{ mM}$], previously redispersed in pure CTAC solution, was centrifuged and redispersed in 4–5 times diluted BINAMINE/CTAC solution and left undisturbed overnight at room temperature. Before further use, Au NRs were washed once again and redispersed in water.

Platinum Overgrowth. In a 2 mL Eppendorf tube, 50 μL of 10 mM K_2PtCl_4 solution was added to a solution containing 600 μL of water and 200 μL of BINAMINE/CTAC solution. A fixed amount of Au NR seed solution was then poured onto the above solution, followed by fast addition of 200 μL of 0.8 M ascorbic acid. The solution was shaken and then kept undisturbed overnight in a water bath at a set temperature, to allow the growth of platinum grooves around Au NRs. Finally, the Au@Pt NR solution was washed twice using water and redispersed in 5 mM CTAC solution.

Transmission Electron Microscopy. Atomic resolution HAADF-STEM imaging, was performed using a Thermo Fisher Scientific Themis Z operated at 300 kV with a camera length of 115 mm. HAADF-STEM, EDX-STEM, and electron tomography experiments were performed using a Thermo Fisher Scientific Osiris electron microscope operated at 200 kV. 2D EDX-STEM data sets were acquired using a Super-X detector with a 150 pA beam current and a total acquisition time of approximately 10 min. The EDX-STEM tomography reconstruction shown in Figure 2 was obtained by collecting EDX data using an Ultra-X detector implemented on an Thermo Fisher Scientific Spectra electron microscope. This detector provides a ~6 \times higher EDX signal across the entire tilt range than a regular quad detector (Super-X) and minimizes the electron dose required to come to a good S/N ratio for the compositional 3D analysis.⁴⁴ The tilt series was acquired within a $\pm 70^\circ$ tilt range and a tilt increment of 10° with a 150 pA beam current and a total time acquisition of approximately 5 min.

Electron Tomography. A DENSolutions Wildfire heating sample holder optimized for electron tomography was used. Tomographic series were acquired within a $\pm 70^\circ$ tilt range and a tilt increment of 3° . To eliminate different image distortions, we applied a convolutional neural network.³⁸ Undistorted images were aligned with respect

594 to each other by using a phase correlation, which was also used to
595 determine the shift and the angle of the rotation axis. 3D
596 reconstruction was performed by an approach consisting of iterating
597 between several SIRT cycles and application of constraints in the real
598 and Fourier space.³⁸ After applying a bandwidth limit to the FFT, the
599 result is transformed to real space, and a threshold is applied to the
600 intensity of the 3D volume. Next, the SIRT cycles are repeated. In this
601 manner, a high-quality 3D reconstruction with diminished missing
602 wedge is obtained.

603 The reconstruction shown in Figure 4 was performed using an
604 expectation–maximization (EM) algorithm, as implemented in Astra
605 Toolbox.⁵⁶

606 **Molecular Dynamics Simulations. Input Structures.** The input
607 Au NR structure was created as suggested by Carbó-Argibay et al.⁴⁷
608 First, an FCC Au structure in a rectangular prism was created. Then,
609 the two base faces of the octagonal prisms were formed by Au {001}
610 facets, and the ends of the prism were truncated to form {011} and
611 {111} facets. Afterward, the lateral facets were truncated according to
612 a {520} configuration.

613 To create Pt-shell around the created input structure of Au NR
614 based on the morphology of 3D reconstructions retrieved by electron
615 tomography, first, the reconstructed volume was binarized by setting
616 the values above a threshold to 1 and setting the others to 0. Here, the
617 threshold value was defined by Otsu's method.⁵⁷ Next, each binarized
618 3D volume was filtered with a 3D Gaussian smoothing kernel to
619 create a mask. At the same time, an FCC Pt structure was created in a
620 rectangular simulation box. Then, Pt structures were extracted by
621 applying the created masks to the FCC rectangular simulation box.
622 Finally, the previously created Au NR was placed at the center of the
623 created Pt structures. Since using the actual size of the experimental
624 NPs in MD simulations requires vast computational power, the overall
625 sizes of the created Au@Pt NRs were scaled down. However, for all
626 the other parameters, such as aspect ratio and Pt/Au ratios,
627 experimentally determined values were used.

628 The surface coverage of the Pt shell was calculated from the ratio
629 between the number of Au surface atoms covered by the Pt-shell and
630 the total number of atoms at the surface of the Au core. Hereby,
631 neighbors of surface Au atoms within a defined cutoff distance, 2.99
632 Å, were defined. If there is at least one Pt atom among the neighbor
633 list of a surface Au atom, that Au atom was counted as covered by Pt-
634 coating.

635 **Simulations.** All the MD simulations were carried out using the
636 program Large-Scale Atomic/Molecular Massively Parallel Simula-
637 tor.⁵⁸ 3D structures were visualized by the OVITO open visualization
638 tool.⁵⁹ The equations of motion were integrated using the velocity
639 Verlet algorithm with a time step of 1 fs. Nonperiodic boundary
640 conditions were applied in all three directions with a large vacuum
641 area. Also, the total linear and angular momenta were conserved so
642 that the rod did not drift nor rotate during our simulation. The
643 simulations were carried out with the EAM potential.⁴⁶

644 First, the conjugate gradient energy minimization was applied to all
645 input structures of NRs by imposing a maximum distance that an
646 atom can move in a one-time step. The maximum displacement
647 distance was first set as 0.01 Å. Afterward, the systems were relaxed at
648 room temperature for 20 ns in a canonical ensemble with Nosé–
649 Hoover thermostat (NVT ensemble) and a damping factor of 0.1.
650 Then, the temperature of each system was increased with the NVT
651 ensemble to the specified temperatures with a constant heating rate of
652 0.5 K/ps, and the NRs were relaxed for 20 ns at each temperature.

653 For the simulation of the Pt islands (111) on the Au surface (111),
654 an Au substrate was created with (111) surface facets and relaxed for
655 10 ns at room temperature. During the relaxation, periodic boundary
656 conditions were applied in the *x* and *y*-directions, and a nonperiodic
657 boundary condition was applied in the *z*-direction. Next, Pt islands
658 with different thicknesses were placed on top of the surface and a full
659 relaxation was performed for 20 ns at room temperature. Then the
660 temperature was increased with a 0.5 K/ps heating rate and relaxed
661 for 20 ns at 200 °C, 400 °C, and 600 °C by using NVT.

ASSOCIATED CONTENT

Supporting Information

The Supporting Information is available free of charge at
<https://pubs.acs.org/doi/10.1021/acsnano.2c02889>.

Movie S1: 3D HAAF STEM reconstruction of sample (1) at room temperature (MPG)	666
Movie S2: 3D HAADF STEM reconstruction of sample (2) at room temperature (MPG)	668
Movie S3: 3D HAADF STEM reconstruction of sample (3) at room temperature (MPG)	670
Movie S4: 3D EDX reconstruction (MPG)	672
Movie S5: In situ HAADF-STEM time series of sample (3) illustrating void formation upon heating (MP4)	673
Movie S6: 3D HAAF STEM reconstruction of sample (1) after being heated up to 200 °C (MPG)	675
Movie S7: 3D HAAF STEM reconstruction of sample (2) after being heated up to 200 °C (MPG)	677
Movie S8: 3D HAAF STEM reconstruction of sample (3) after being heated up to 200 °C (MPG)	679
Detailed description of Au@Pt NPs colloidal synthesis. Statistical analysis of HAADF-STEM images. Additional EDX-STEM mappings of the depleted Au and the Pt shell after annealing. Analysis of Au NRs with high index facets using electron tomography and 3D fast Fourier transform. MD simulations of spherical Au–Pt NPs. Extra input structures used in the MD simulations. MD simulations of an Au@Pt NR with a continuous Pt-shell (PDF)	681

AUTHOR INFORMATION

Corresponding Authors

Sara Bals – EMAT, University of Antwerp, 2020 Antwerp, Belgium; NANOLab Center of Excellence, University of Antwerp, 2020 Antwerp, Belgium; orcid.org/0000-0002-4249-8017; Email: sara.bals@uantwerpen.be

Luis M. Liz-Marzán – CIC biomaGUNE, Basque Research and Technology Alliance (BRTA), 20014 Donostia-San Sebastián, Spain; Ikerbasque, Basque Foundation for Science, 48009 Bilbao, Spain; Biomedical Research Networking Center in Bioengineering, Biomaterials, and Nanomedicine (CIBER-BBN), 20014 Donostia-San Sebastián, Spain; orcid.org/0000-0002-6647-1353; Email: llizmarzan@cicbiomagune.es

Authors

Adrián Pedraza-Tardajos – EMAT, University of Antwerp, 2020 Antwerp, Belgium; NANOLab Center of Excellence, University of Antwerp, 2020 Antwerp, Belgium

Ece Arslan Irmak – EMAT, University of Antwerp, 2020 Antwerp, Belgium; NANOLab Center of Excellence, University of Antwerp, 2020 Antwerp, Belgium

Vished Kumar – CIC biomaGUNE, Basque Research and Technology Alliance (BRTA), 20014 Donostia-San Sebastián, Spain

Ana Sánchez-Iglesias – CIC biomaGUNE, Basque Research and Technology Alliance (BRTA), 20014 Donostia-San Sebastián, Spain; Biomedical Research Networking Center in Bioengineering, Biomaterials, and Nanomedicine (CIBER-BBN), 20014 Donostia-San Sebastián, Spain; orcid.org/0000-0003-1871-8742

- 720 **Qiongyang Chen** – EMAT, University of Antwerp, 2020
721 Antwerp, Belgium; NANOLab Center of Excellence,
722 University of Antwerp, 2020 Antwerp, Belgium
- 723 **Maarten Wirix** – Thermo Fisher Scientific, 5651 Eindhoven,
724 The Netherlands
- 725 **Bert Freitag** – Thermo Fisher Scientific, 5651 Eindhoven, The
726 Netherlands
- 727 **Wiebke Albrecht** – EMAT, University of Antwerp, 2020
728 Antwerp, Belgium; NANOLab Center of Excellence,
729 University of Antwerp, 2020 Antwerp, Belgium
- 730 **Sandra Van Aert** – EMAT, University of Antwerp, 2020
731 Antwerp, Belgium; NANOLab Center of Excellence,
732 University of Antwerp, 2020 Antwerp, Belgium
- 733 Complete contact information is available at:
734 <https://pubs.acs.org/10.1021/acsnano.2c02889>
- 735 **Author Contributions**
- 736 #A.P.-T. and E.A.I. contributed equally. A.P.-T. performed EM
737 characterization and analysis. E.A.I. executed and analyzed the
738 MD simulations. A.S.-I. and V.K. performed the NP synthesis.
- 739 Q.C., M.W. and B.F. performed the 3D EDX-STEM
740 acquisition and 3D reconstruction using an Ultra-X detector.
- 741 W.A., S.V.A., L.M.L.-M. and S.B. supervised the project. The
742 manuscript was written through contributions of all authors.
- 743 **Notes**
- 744 The authors declare no competing financial interest.
- 745 **ACKNOWLEDGMENTS**
- 746 S.B., S.V.A., L.M.L.-M. and A.P.-T. acknowledge financial
747 support from the European Commission under the Horizon
748 2020 Programme by grant nos. 731019 (EUSMI) and 823717
749 (ESTEEM3) and ERC Consolidator grant nos. 815128
750 (REALNANO) and 770887 (PICOMETRICS). L.M.L.-M.
751 acknowledges funding from MCIN/AEI/10.13039/
752 501100011033 through grants no. PID2020-117779RB-I00
753 and Maria de Maeztu Unit of Excellence no. MDM-2017-0720.
754 The authors acknowledge the resources and services used for
755 the simulations in this work were provided by the VSC
756 (Flemish Supercomputer Center), funded by the Research
757 Foundation - Flanders (FWO) and the Flemish Government.
- 758 **REFERENCES**
- 759 (1) Wang, D.; Li, Y. Bimetallic Nanocrystals: Liquid-Phase Synthesis
760 and Catalytic Applications. *Adv. Mater.* **2011**, *23*, 1044–1060.
- 761 (2) DeSantis, C. J.; Weiner, R. G.; Radmilovic, A.; Bower, M. M.;
762 Skrabalak, S. E. Seeding Bimetallic Nanostructures as a New Class of
763 Plasmonic Colloids. *J. Phys. Chem. Lett.* **2013**, *4*, 3072–3082.
- 764 (3) Gilroy, K. D.; Ruditskiy, A.; Peng, H. C.; Qin, D.; Xia, Y.
765 Bimetallic Nanocrystals: Syntheses, Properties, and Applications.
766 *Chem. Rev.* **2016**, *116*, 10414–10472.
- 767 (4) Leary, R. K.; Kumar, A.; Straney, P. J.; Collins, S. M.; Yazdi, S.;
768 Dunin-Borkowski, R. E.; Midgley, P. A.; Millstone, J. E.; Ringe, E.
769 Structural and optical properties of discrete dendritic Pt nanoparticles
770 on colloidal Au nanoprisms. *J. Phys. Chem. C* **2016**, *120*, 20843–
771 20851.
- 772 (5) Liz-Marzán, L. M. Tailoring Surface Plasmons through the
773 Morphology and Assembly of Metal Nanoparticles. *Langmuir.* **2006**,
774 *22*, 32–41.
- 775 (6) Pérez-Juste, J.; Pastoriza-Santos, I.; Liz-Marzán, L. M.;
776 Mulvaney, P. Gold nanorods: Synthesis, characterization and
777 applications. *Coord. Chem. Rev.* **2005**, *249*, 1870–1901.
- 778 (7) Zorić, I.; Zäch, M.; Kasemo, B.; Langhammer, C. Gold,
779 Platinum, and Aluminum Nanodisk Plasmons: Material Independ-
- ence, Subradiance, and Damping Mechanisms. *ACS Nano* **2011**, *5*,
2535–2546.
- (8) He, W.; Liu, Y.; Yuan, J.; Yin, J. J.; Wu, X.; Hu, X.; Zhang, K.;
Liu, J.; Chen, C.; Ji, Y.; Guo, Y. Au@Pt nanostructures as oxidase and
peroxidase mimetics for use in immunoassays. *Biomaterials.* **2011**, *32*,
1139–1147.
- (9) Zhao, Y.; Ye, C.; Liu, W.; Chen, R.; Jiang, X. Tuning the
composition of AuPt bimetallic nanoparticles for antibacterial
application. *Angew. Chem., Int. Ed.* **2014**, *53*, 8127–8131.
- (10) Wang, S.; Kristian, N.; Jiang, S.; Wang, X. Controlled
deposition of Pt on Au nanorods and their catalytic activity towards
formic acid oxidation. *Electrochemistry Communications. Electro-*
chem. commun. **2008**, *10*, 961–964.
- (11) Iyyamperumal, R.; Zhang, L.; Henkelman, G.; Crooks, R. M.
Efficient Electrocatalytic Oxidation of Formic Acid using Au@Pt
Dendrimer-Encapsulated Nanoparticles. *J. Am. Chem. Soc.* **2013**, *135*,
5521–5524.
- (12) Tian, N.; Zhou, Z.-Y.; Sun, S.-G.; Ding, Y.; Wang, Z. L.
Synthesis of tetrahedral platinum nanocrystals with high-index
facets and high electro-oxidation activity. *Science.* **2007**, *316*, 732–
735.
- (13) Zhou, Z.-Y.; Tian, N.; Li, J.-T.; Broadwell, I.; Sun, S.-G.
Nanomaterials of high surface energy with exceptional properties in
catalysis and energy storage. *Chem. Soc. Rev.* **2011**, *40*, 4167–4185.
- (14) Zhang, Q.; Wang, H. Facet-Dependent Catalytic Activities of
Au Nanoparticles Enclosed by High-Index Facets. *ACS Catal.* **2014**, *4*,
4027–4033.
- (15) Albrecht, W.; van der Hoeven, J. E. S.; Deng, T.-S.; de Jongh, P.
E.; van Blaaderen, A. Fully alloyed metal nanorods with highly tunable
properties. *Nanoscale.* **2017**, *9*, 2845–2851.
- (16) Fennell, J.; He, D.; Tanyi, A. M.; Logsdail, A. J.; Johnston, R.
L.; Li, Z. Y.; Horswell, S. L. A Selective Blocking Method To Control
the Overgrowth of Pt on Au Nanorods. *J. Am. Chem. Soc.* **2013**, *135*,
6554–6561.
- (17) Straney, P. J.; Marbella, L. E.; Andolina, C. M.; Nuhfer, N. T.;
Millstone, J. E. Decoupling mechanisms of platinum deposition on
colloidal gold nanoparticle substrates. *J. Am. Chem. Soc.* **2014**, *136*
(22), 7873–7876.
- (18) Grzelczak, M.; Pérez-Juste, J.; Rodríguez-González, B.; Liz-
Marzán, L. M. Influence of silver ions on the growth mode of
platinum on gold nanorods. *J. Mater. Chem.* **2006**, *16*, 3946–3951.
- (19) Xu, Z.; Carlton, C. E.; Allard, L. F.; Shao-Horn, Y.; Hamad-
Schifferli, K. Direct Colloidal Route for Pt-Covered AuPt Bimetallic
Nanoparticles. *J. Phys. Chem. Lett.* **2010**, *1*, 2514–2518.
- (20) Aataee-Esfahani, H.; Wang, L.; Nemoto, Y.; Yamauchi, Y.
Synthesis of Bimetallic Au@Pt Nanoparticles with Au Core and
Nanostructured Pt Shell toward Highly Active Electrocatalysts. *Chem.*
Mater. **2010**, *22*, 6310–6318.
- (21) Habas, S. E.; Lee, H.; Radmilovic, V.; Somorjai, G. A.; Yang, P.
Shaping binary metal nanocrystals through epitaxial seeded growth.
Nat. Mater. **2007**, *6*, 692–697.
- (22) Suntivich, J.; Xu, Z.; Carlton, C. E.; Kim, J.; Han, B.; Lee, S. W.;
Bonnet, N.; Marzari, N.; Allard, L. F.; Gasteiger, H. A.; Hamad-
Schifferli, K.; Shao-Horn, Y. Surface composition tuning of Au-Pt
bimetallic nanoparticles for enhanced carbon monoxide and methanol
electro-oxidation. *J. Am. Chem. Soc.* **2013**, *135*, 7985–7991.
- (23) Garcia-Gutierrez, D. I.; Gutierrez-Wing, C. E.; Giovanetti, L.;
Ramallo-López, J. M.; Requejo, F. G.; Jose-Yacamán, M. Temperature
Effect on the Synthesis of Au–Pt Bimetallic Nanoparticles. *J. Phys.*
Chem. B **2005**, *109*, 3813–3821.
- (24) Feng, L.; Wu, X.; Ren, L.; Xiang, Y.; He, W.; Zhang, K.; Zhou,
W.; Xie, S. Well-Controlled Synthesis of Au@Pt Nanostructures by
Gold-Nanorod-Seeded Growth. *Chem.—Eur. J.* **2008**, *14*, 9764–9771.
- (25) Chi, M.; Wang, C.; Lei, Y.; Wang, G.; Li, D.; More, K. L.;
Lupini, A.; Allard, L. F.; Markovic, N. M.; Stamenkovic, V. R. Surface
faceting and elemental diffusion behaviour at atomic scale for alloy
nanoparticles during in situ annealing. *Nat. Commun.* **2015**, *6*, 8925.
- (26) Gonzalez-Rubio, G.; Mosquera, D. J.; Kumar, V.; Pedraza-
Tardajos, A.; Llombart, P.; Solis, D. M.; Lobato, I.; Noya, E. G.; 848

- 849 Guerrero-Martinez, A.; Taboada, J. M.; Obelleiro, F.; MacDowell, L.
850 G.; Bals, S.; Liz-Marzan, L. M. Micelle-directed chiral seeded growth
851 on anisotropic gold nanocrystals. *Science*. **2020**, *368*, 1472–1477.
- 852 (27) Plodinec, M.; Nerl, H. C.; Girgsdies, F.; Schlögl, R.;
853 Lunkenbein, T. Insights into Chemical Dynamics and Their Impact
854 on the Reactivity of Pt Nanoparticles during CO Oxidation by
855 Operando TEM. *ACS Catalysis*. **2020**, *10*, 3183–3193.
- 856 (28) Deng, L.; Hu, W.; Deng, H.; Xiao, S. Surface Segregation and
857 Structural Features of Bimetallic Au–Pt Nanoparticles. *J. Phys. Chem.*
858 *C* **2010**, *114*, 11026–11032.
- 859 (29) Joo, S. H.; Park, J. Y.; Tsung, C. K.; Yamada, Y.; Yang, P.;
860 Somorjai, G. A. Thermally stable Pt/mesoporous silica core-shell
861 nanocatalysts for high-temperature reactions. *Nat. Mater.* **2009**, *8*,
862 126–131.
- 863 (30) Wen, Y.-H.; Huang, R.; Li, C.; Zhu, Z.-Z.; Sun, S.-G. Enhanced
864 thermal stability of Au@Pt nanoparticles by tuning shell thickness:
865 Insights from atomistic simulations. *J. Mater. Chem.* **2012**, *22*, 7380–
866 7386.
- 867 (31) He, D. S.; Han, Y.; Fennell, J.; Horswell, S. L.; Li, Z. Y. Growth
868 and stability of Pt on Au nanorods. *Appl. Phys.* **2012**, *101*, 113102.
- 869 (32) Albrecht, W.; Van Aert, S.; Bals, S. Three-Dimensional
870 Nanoparticle Transformations Captured by an Electron Microscope.
871 *Acc. Chem. Res.* **2021**, *54*, 1189–1199.
- 872 (33) van der Hoeven, J. E.; Welling, T. A.; Silva, T. A.; van den
873 Reijen, J. E.; La Fontaine, C.; Carrier, X.; Louis, C.; van Blaaderen, A.
874 J.; de Jongh, P. E. In situ observation of atomic redistribution in
875 alloying gold–silver nanorods. *ACS Nano* **2018**, *12*, 8467–8476.
- 876 (34) Vanrompay, H.; Bladt, E.; Albrecht, W.; Béché, A.; Zakhozheva,
877 M.; Sánchez-Iglesias, A.; Liz-Marzán, L. M.; Bals, S. 3D character-
878 ization of heat-induced morphological changes of Au nanostars by fast
879 in situ electron tomography. *Nanoscale*. **2018**, *10*, 22792–22801.
- 880 (35) Skorikov, A.; Albrecht, W.; Bladt, E.; Xie, X.; van der Hoeven, J.
881 E.; van Blaaderen, A.; Van Aert, S.; Bals, S. Quantitative 3D
882 Characterization of Elemental Diffusion Dynamics in Individual Ag@
883 Au Nanoparticles with Different Shapes. *ACS Nano* **2019**, *13*, 13421–
884 13429.
- 885 (36) Albrecht, W.; Bladt, E.; Vanrompay, H.; Smith, J. D.; Skrabalak,
886 S. E.; Bals, S. Thermal Stability of Gold/Palladium Octopods Studied
887 in Situ in 3D: Understanding Design Rules for Thermally Stable
888 Metal Nanoparticles. *ACS Nano* **2019**, *13*, 6522–6530.
- 889 (37) Bagiński, M.; Pedraza-Tardajos, A.; Altantzis, T.; Tupikowska,
890 M.; Vetter, A.; Tomczyk, E.; Suryadharna, R. N. S.; Pawlak, M.;
891 Andruszkiewicz, A.; Górecka, E.; Pocięcha, D.; Rockstuhl, C.; Bals, S.;
892 Lewandowski, W. Understanding and Controlling the Crystallization
893 Process in Reconfigurable Plasmonic Superlattices. *ACS Nano* **2021**,
894 *15*, 4916–4926.
- 895 (38) Altantzis, T.; Lobato, I.; De Backer, A.; Béché, A.; Zhang, Y.;
896 Basak, S.; Porcu, M.; Xu, Q.; Sánchez-Iglesias, A.; Liz-Marzán, L. M.;
897 Van Tendeloo, G.; Van Aert, S.; Bals, S. Three-Dimensional
898 Quantification of the Facet Evolution of Pt Nanoparticles in a
899 Variable Gaseous Environment. *Nano Lett.* **2019**, *19*, 477–481.
- 900 (39) Arslan Irmak, E.; Liu, P.; Bals, S.; Van Aert, S. 3D Atomic
901 Structure of Supported Metallic Nanoparticles Estimated from 2D
902 ADF STEM Images: A Combination of Atom-Counting and a Local
903 Minima Search Algorithm. *Small Methods. Small Methods.* **2021**, *5*,
904 2101150.
- 905 (40) Petrova, H.; Juste, J. P.; Pastoriza-Santos, I.; Hartland, G. V.;
906 Liz-Marzán, L. M.; Mulvaney, P. (2006). On the temperature stability
907 of gold nanorods: comparison between thermal and ultrafast laser-
908 induced heating. *PCCP*. **2006**, *8*, 814–821.
- 909 (41) Mychinko, M.; Skorikov, A.; Albrecht, W.; Sánchez-Iglesias, A.;
910 Zhuo, X.; Kumar, V.; Liz-Marzán, L.; Bals, S. The influence of size,
911 shape, and twin boundaries on heat-induced alloying in individual
912 Au@Ag core–shell nanoparticles. *Small*. **2021**, *17*, 2102348.
- 913 (42) Wang, Z. L.; Petroski, J. M.; Green, T. C.; El-Sayed, M. A.
914 Shape transformation and surface melting of cubic and tetrahedral
915 platinum nanocrystals. *J. Phys. Chem. B* **1998**, *102*, 6145–6151.
- 916 (43) Buffat, Ph.; Borel, J.-P. Size effect on the melting temperature of
917 gold particles. *Phys. Rev. A* **1976**, *13*, 2287–2298.
- (44) Zaluzec, N. First Light on the Argonne PicoProbe and The X-
ray Perimeter Array Detector (XPAD). *Microsc. Microanal.* **2021**, *27*,
2070–2074.
- (45) van Omme, J. T.; Zakhozheva, M.; Spruit, R. G.; Sholkina, M.;
Pérez Garza, H. H. Advanced microheater for in situ transmission
electron microscopy; enabling unexplored analytical studies and
extreme spatial stability. *Ultramicroscopy*. **2018**, *192*, 14–20.
- (46) O'Brien, C. J.; Barr, C. M.; Price, P. M.; Hattar, K.; Foiles, S. M.
Grain boundary phase transformations in PtAu and relevance to
thermal stabilization of bulk nanocrystalline metals. *J. Mater. Sci.*
2018, *53*, 2911–2927.
- (47) Carbó-Argibay, E.; Rodríguez-González, B.; Gómez-Graña, S.;
Guerrero-Martínez, A.; Pastoriza-Santos, I.; Pérez-Juste, J.; Liz-
Marzán, L. M. The Crystalline Structure of Gold Nanorods Revisited:
Evidence for Higher-Index Lateral Facets. *Angew. Chem., Int. Ed.*
2010, *49*, 9397–9400.
- (48) Kittel, C. *Introduction to Solid State Physics*, 8th ed.; Wiley &
Sons: New York, NY, 2004.
- (49) Eom, N.; Messing, M. E.; Johansson, J.; Deppert, K. General
Trends in Core–Shell Preferences for Bimetallic Nanoparticles. *ACS*
Nano **2021**, *15* (5), 8883–8895.
- (50) Wang, L. L.; Johnson, D. D. Predicted trends of core-shell
preferences for 132 late transition-metal binary-alloy nanoparticles. *J.*
Am. Chem. Soc. **2009**, *131* (39), 14023–14029.
- (51) Liu, H. B.; Pal, U.; Ascencio, J. A. Thermodynamic Stability and
Melting Mechanism of Bimetallic Au–Pt Nanoparticles. *J. Phys. Chem.*
C **2008**, *112*, 19173–19177.
- (52) Nilekar, A. U.; Ruban, A. V.; Mavrikakis, M. Surface segregation
energies in low-index open surfaces of bimetallic transition metal
alloys. *Surf. Sci.* **2009**, *603*, 91–96.
- (53) Ferrando, R.; Jellinek, J.; Johnston, R. L. Nanoalloys: From
Theory to Applications of Alloy Clusters and Nanoparticles. *Chem.*
Rev. **2008**, *108*, 845–910.
- (54) Ye, X.; Zheng, C.; Chen, J.; Gao, Y.; Murray, C. B. Using binary
surfactant mixtures to simultaneously improve the dimensional
tunability and monodispersity in the seeded growth of gold nanorods.
Nano Lett. **2013**, *13*, 765–771.
- (55) González-Rubio, G.; Kumar, V.; Llombart, P.; Díaz-Núñez, P.;
Bladt, E.; Altantzis, T.; Bals, S.; Peña-Rodríguez, O.; Noya, E. G.;
MacDowell, L. G.; et al. Disconnecting Symmetry Breaking from
Seeded Growth for the Reproducible Synthesis of High Quality Gold
Nanorods. *ACS Nano* **2019**, *13*, 4424–4435.
- (56) Van Aarle, W.; Palenstijn, W. J.; De Beenhouwer, J.; Altantzis,
T.; Bals, S.; Batenburg, K. J.; Sijbers, J. The ASTRA Toolbox: A
platform for advanced algorithm development in electron tomog-
raphy. *Ultramicroscopy*. **2015**, *157*, 35–47.
- (57) Otsu, N. A Threshold Selection Method from Gray-Level
Histograms. *IEEE Transactions on Systems, Man, and Cybernetics* **1979**,
9 (1), 62–66.
- (58) Thompson, A. P.; et al. LAMMPS - a flexible simulation tool
for particle-based materials modeling at the atomic, meso, and
continuum scales. *Comput. Phys. Commun.* **2022**, *271*, 108171.
- (59) Stukowski, A. Visualization and analysis of atomistic simulation
data with OVITO-the Open Visualization Tool. *Model. Simul. Mater.*
Sci. Eng. **2010**, *18*, No. 015012.